ADVANCED ENERGY MATERIALS
www.advenergymat.de

Suppressed Degradation Process of Green-Solvent Based Organic Solar Cells Through ZnO Modification With Sulfhydryl Derivatives

*Zerui Li, Yunan Li, Jinsheng Zhang, Renjun Guo, Kun Sun, Xiongzhuo Jiang, Peixi Wang, Suo Tu, Matthias Schwartzkopf, Zhiyun Li, Chang-Qi Ma, and Peter Müller-Buschbaum**

The interface of organic solar cells plays a crucial role in device performance and stability. Several investigations demonstrated that the interface will affect the morphology and microstructure of the active layer, which is important for device performance. Here, several mercaptan derivatives are explored in green-solvent based organic solar cells (PBDB-TF-T1: BTP-4F-12) as effective stabilization modifiers on ZnO. *Operando* grazing-incidence wide/small-angle X-ray scattering (GIWAXS/GISAXS) provides a deep understanding of the degradation process during operation. The degradation process is driven by a compression of the molecule stacking as well as a decrease in the donor crystallinity, besides the known decomposition of the acceptor at the interface. Solar cell degradation comprises three stages, where an unexpected component from the acceptor appears in the second stage, simultaneously with a shapely shrinking micro-structure. Furthermore, the interface modifier pentaerythritol tetrakis(3-mercapto-propionate) (PETMP) stabilizes the crystallinity of the donor as well as suppresses the decomposition of the acceptor, thus improving the device stability. The modification effect is caused by the interaction between Zn and S from the sulfhydryl groups of the mercaptan derivatives. Thus, studies of changes in the active layer morphology extend the knowledge from ex situ characterizations, broadening the understanding of the degradation mechanisms.

1. Introduction

The rapid development of non-fullerene acceptors has greatly promoted the efficiency of organic solar cells, which has reached over 19%.[1] Nowadays, the relatively poor stability has raised up as another research hot spot for organic solar cells. The degradation of organic solar cells can be caused by a multitude of different factors such as light, heat, mechanical stress, oxygen, and moisture.[2] Understanding the complex mechanisms of device degradation is of high importance. While classical ex situ measurements can only offer limited information for the fresh and aged states, operando measurements have been proven to be a useful tool for the kinetic analysis of degradation processes. In particular, operando grazing-incidence wide/small-angle X-ray scattering (GIWAXS/GISAXS) provides information about the evolution of the crystallinity and the microstructure during the device degradation process.[3] In the complex functional stack forming the solar cell, the sensitive interface of ZnO was found to be highly related to the morphology and crystallinity of the active layer and, therefore, of importance for the device performance.[4] For example, Su et.al found that the morphology of the active layer would also be influenced with the interfacial modification of ZnO with plasmonic gold nanoparticles (NPs) at an amphiphilic dendritic block copolymer (DBC)

Z. Li, J. Zhang, R. Guo, K. Sun, X. Jiang, P. Wang, S. Tu, P. Müller-Buschbaum
TUM School of Natural Sciences
Department of Physics
Chair for Functional Materials
Technical University of Munich
James-Franck-Str. 1, 85748 Garching, Germany
E-mail: muellerb@ph.tum.de

The ORCID identification number(s) for the author(s) of this article can be found under https://doi.org/10.1002/aenm.202402920

DOI: 10.1002/aenm.202402920

Z. Li, Y. Li, C.-Q. Ma
i-Lab & Printable Electronics Research Center
Suzhou Institute of Nano-Tech and Nano-Bionics
Chinese Academy of Sciences (CAS)
Ruoshui Road 398, SEID, SIP, Suzhou 215123, China

R. Guo
Karlsruhe Institute of Technology (KIT)
Institute of Microstructure Technology
Herrmann-von-Helmholtz-Platz 1, 76344 Karlsruhe, Germany

M. Schwartzkopf
Deutsches Elektronen-Synchrotron DESY
Notkestr. 85, 22607 Hamburg, Germany

Z. Li
Vacuum Interconnected Nanotech Workstation
Suzhou Institute of Nano-Tech and Nano-Bionics
Chinese Academy of Sciences (CAS)
Ruoshui Road 398, SEID, SIP, Suzhou 215123, China

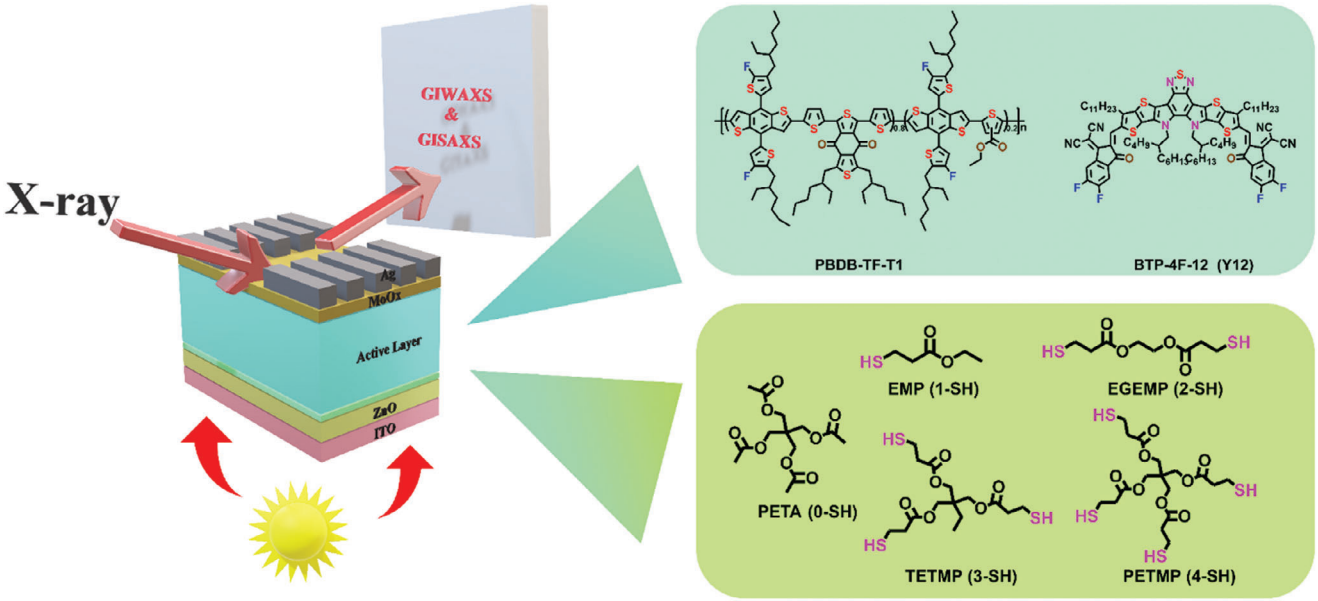

Figure 1. a) Scheme of the operando GISAXS/GIWAXS measurements of organic solar cells; b) an active layer of PBDB-TF-T1 and BTP-4F-12 and c) the chemical structures of studied interfacial modifiers.

denoted as DBC@AuNPs.[5] Li et.al got an efficient and stable organic solar cell using $ZrSe_2$ modified ZnO, where the crystallinity of PBDB-T:ITIC increased due to the modification.[6] Besides a simple performance decrease, the interfacial degradation at the ZnO/active layer interface under illumination was also reported to be the key issue for device aging caused by the decomposition of the organic active layer due to a photocatalytic effect.[7] Furthermore, such interfacial degradation could be effectively suppressed with interfacial modifications using several different chemical approaches such as self-assembled monolayers (SAM) [8], a pyrene-bodipy molecular dye (Py-BDP),[9] fullerene derivatives,[10] hydroxide and/or hydroxyl radical scavengers, e.g., ethylenediamine-tetraacetic acid (EDTA), isopropyl alcohol (IPA), and 2-phenylethanethiol (2-PET).[7c] Although 2-PET showed the best interfacial modification effect, the chemistry working principle behind this improvement is not clear yet. Moreover, 2-PET is highly toxic with a bad smell, which renders it less attractive during device fabrication.

Another issue calling the attention of scientists is environmental-friendly organic solar cells. To become environmental-friendly the used solvents are a key factor. Today, still the most used solvents are halogenated solvents such as chloroform, chlorobenzene and 1,2,4-trichlorobenzene or aromatic solvents (e.g., toluene, o-xylene, 1,2,4-trimethyl-benzene).[11] In addition, also halogenated additives (e.g., 1-chloro-naphthalene and 1,8-diiodooctane) are frequently used. These chemicals would harm the human body and can cause environmental pollution during the device fabrication process and waste solvent treatment. Accordingly, in the present study, materials that could work well in tetrahydrofuran (THF) are chosen as the research model, where the conjugated polymer PBDB-TF-T1 and the non-fullerene small molecule BTP-4F-12 are used as donor and acceptor, with diphenyl ether (DPE) as additive. THF has relatively lower toxicity compared with traditional halogenated or aromatic solvents and shows great potential in the case of alkanes when used as a green solvent for organic solar cell fabrication.

Because 2-PET is of high toxicity with an unclear interface modification mechanism in our present work, a series of alternatives for 2-PET is explored for modification. The five selected molecules have different amounts of mercapto groups, ranging from 0 to 4 sulfhydryl groups (-SH), and are named pentaerythritol tetraacetate (PETA), butyl 3-mercaptopropionate (BMP), ethylene glycol bis(3-mercaptopropionate) (EGBMP), trimethylolpropane tris(3-mercaptopropionate) (TETMP), pentaerythritol tetrakis(3-mercapto-propionate) (PETMP) (see **Figure 1**). The device performance, as well as the light stability, are investigated. We observe that the ZnO modification with molecules having more sulfhydryl groups, i.e., using TETMP and PETMP, results in an optimized device performance and stability, suggesting a key role of sulfhydryl groups. Operando GIWAXS and GISAXS measurements probe the device degradation in air to deeply investigate the differences in the degradation processes between PETMP modified solar cells and reference ones. A three-stage degradation process is found for the reference solar cell, and the PETMP modification suppresses the decomposition of the acceptor and the decrease of the polymer donor crystallinity. XPS is used to analyze the element distribution on the ZnO surface, where the ratio of hydroxyl oxygen decreases with sulfhydryl derivatives, which supports the assumed degradation mechanism that hydroxyl causes the interfacial degradation. With FTIR the interaction between PETMP and ZnO is probed. The -SH signal disappears after mixing the two compounds, which demonstrates the interaction between -SH and Zn^{2+}, supporting the importance of -SH in the interfacial modification. Here, GISAXS and GIWAXS provide valuable information about kinetic changes in the active layers of the solar cells during the device degradation,

which goes well beyond a simple interface degradation and modification.

2. Results and Discussion

Figure 1 shows the device structure as well as the chemicals used in this work, where an inverted structure of ITO/ZnO/active layer/MoO_3/Ag is selected as model solar cell. THF and DPE are selected as the solvent and additive to align with a green solar cell fabrication, respectively. THF has less toxicity compared with the traditional halogenated and aromatic solvents commonly used in the preparation of active layer solutions, which could decrease the damage to human body and environment during the device fabrication and waste treatment and offer more potential in real applications. In addition, the similar boiling points of chloroform (61.2 °C) and THF (66 °C) demonstrate the similar solvent evaporation rate as well as film formation process, suggesting that it will not affect the device performance and stability if an optimized microstructure and morphology of active layer film is achieved. For better solubility in the green solvent, we select the conjugated polymer PBDB-TF-T1 as the donor (see Figure 1), which comprises PBDB-TF and PTO2 with an optimized ratio of 0.8:0.2.[12] PTO2 was introduced to enhance solubility in non-aromatic solvents without significantly impacting device performance compared to the traditional donor polymer PBDB-T-2F (also known as PM6). The non-fullerene small molecule BTP-4F-12 (or Y12, see Figure 1) is selected due to its excellent solubility coming from longer side chains compared with BTP-4F.[12b,13] It was reported that PBDB-TF-T1:BTP-4F-12 could serve as a reliable material system in THF with excellent performance.[12]

In our previous study, we observed that the interfacial degradation coming from the photocatalyst effect of ZnO is the key reason causing the device degradation, where 2-PET showed an excellent effect on improving the device stability via eliminating interfacial hydroxide or hydroxyl radicals.[7c,14] In the present study, several mercaptan derivatives are selected as alternatives for 2-PET (see Figure 1) for the interface modification, and methanol is maintained as a solvent for the interfacial modifier. In the first set of experiments, PETMP is used in the classical system PBDB-T-2F:BTP-4F (PM6:Y6) to establish an optimized process. The achieved device performance with different PETMP concentrations is shown in Figure S1 and Table S1 (Supporting Information). An excessive interface modification results in solar cells showing an S-shape *J-V* curve, suggesting that the interfacial charge transfer or injection is suppressed. As a result, an optimized concentration of 0.2 mg mL^{-1} in methanol is got, which is kept constant for the subsequent work.

When using the mercaptan derivatives (with 0.2 mg mL^{-1}) as interfacial modifiers of the ZnO/active layer interface pronounced differences in the solar cell performance is found. The detailed solar cell performance data are listed in **Table 1** and plotted in Figure S2 (Supporting Information). Again, methanol (MeOH) is used as a reference for the interface modifiers to exclude the effect from the used solvent of the mercaptan derivatives. The device performance of MeOH modified solar cells increased a bit from 13.6 to 14.1% compared with the reference devices without interface modification (w/o). A further improved device efficiency is achieved with TETMP and PETMP modification (increase to 14.4%). In contrast, there are no obvious differences between the reference and modifiers with fewer sulfhydryl groups (PETA, EMP, EGEMP) in the device efficiency. Almost no obvious change in V_{OC} and J_{SC} is found for these modifiers, and the performance increase mainly results from an increase in the FF, suggesting that the suppressed charge recombination might come from the interface passivation.

Table 1. Device performance of solar cells with different interfacial modifiers.

	V_{OC} [V]	J_{SC} [mA cm^{-2}]	FF	PCE [%]s
w/o	0.831 ± 0.002	24.7 ± 0.2	0.66 ± 0.02	13.6 ± 0.5
MeOH	0.832 ± 0.001	24.8 ± 0.4	0.68 ± 0.01	14.1 ± 0.2
PETA (0-SH)	0.834 ± 0.001	25.1 ± 0.2	0.67 ± 0.01	13.9 ± 0.2
EMP (1-SH)	0.832 ± 0.002	24.2 ± 0.3	0.69 ± 0.02	13.8 ± 0.5
EGEMP (2-SH)	0.831 ± 0.002	24.6 ± 0.4	0.69 ± 0.01	14.1 ± 0.4
TETMP (3-SH)	0.827 ± 0.002	24.9 ± 0.6	0.70 ± 0.01	14.4 ± 0.3
PETMP (4-SH)	0.828 ± 0.002	25.2 ± 0.4	0.69 ± 0.01	14.3 ± 0.4

The average PCE values with standard deviations are calculated from at least 15 devices. All devices are tested with a metal mask applied (effective area of 0.079 cm^2)

The stability of solar cells under illumination in air reveals accelerated degradation processes influenced by the presence of oxygen, with notable differences observed among various interfacial modifiers, highlighting superior stability in TETMP and PETMP modified devices. The stability of these solar cells is investigated under illumination in air with a controlled atmosphere (25-27 °C, 28–32% R.H.). The observed device degradation behavior in terms of V_{OC}, J_{SC}, FF and PCE decrease is shown in **Figure 2**a,d, respectively. All these solar cells show similar but accelerated degradation processes compared with our previous research in nitrogen, where the degradation mainly resulted from losses in J_{SC} and FF.[7c,14] Thus, the presence of oxygen modifies the device degradation. Unexpectedly, PETA modified solar cells show the fastest degradation process compared with the other interface modifiers, including the reference. MeOH modified solar cells show a slight improvement in stability compared to the reference, which matches our earlier findings from degradation studies in the N_2 atmosphere.[7c] For the other four mercaptan derivatives, the device stability improves with the number of sulfhydryl groups. TETMP and PETMP modified solar cells show the best device stability. Both maintain over 70% of their initial PCE values after 15 hours of illumination in air, while the reference decreases to 23%. The calculated T_{80} time is 440 min for TETMP and PETMP compared to 35 min for the reference. The temporal evolution of J_{SC}, V_{OC}, FF, and PCE for each cell are compared in Figure S3 (Supporting Information). For the reference case, the degradation mainly comes from the decay of J_{SC} and FF, while V_{OC} only shows a slight decay, which can be suppressed with MeOH modification, suggesting that such a decay is not attributed to the decrease of the built-in potential.[15] The fast decay of the FF comes from the increased recombination, which might be due to the raddled interface between the active layer and charge transfer layers or the decrease in domain sizes and loss in connectivity of the donor/acceptor during aging.[7,14–16] The fast decay of J_{SC} might come from the decomposition of the

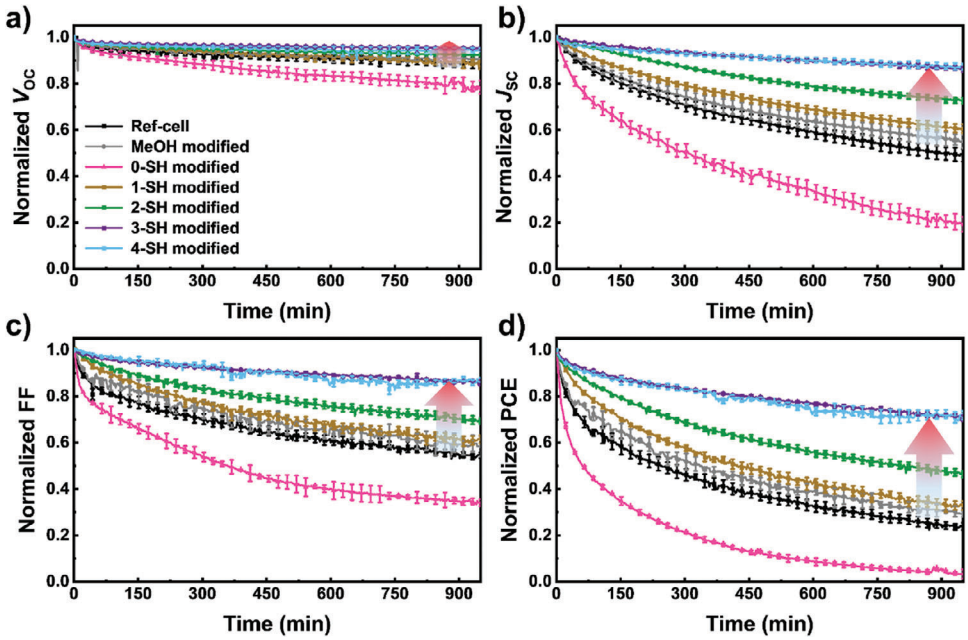

Figure 2. Temporal evolution of PBDB-TF-T1:BTP-4F-12 solar cells (at least 3 pixels) parameters extracted from *J-V* curves under illumination in air (25–27 °C, 28–32% R.H.): a) V_{OC}, b) J_{SC}, c) FF and d) PCE. The different interfacial modifiers are indicated.

acceptor at the interface or the increase of domain sizes and distances in the internal due to the evaporation of additive during operation.[3a–c,7c,14]

Furthermore, mercaptan derivatives modification can suppress the decay of J_{SC} and FF simultaneously, demonstrating that such an improvement works on the interface to suppress the acceptor decomposition with the same effect as 2-PET.[7c] TETMP/PETMP modified solar cells still show an inevitable decrease in J_{SC} and FF. The decreased FF might come from the decrease of polymer domains due to the evaporation of additives during operation, while the loss of J_{SC} might come from the decrease of the crystallinity during the operation time, which we will discuss later in the X-ray scattering part.[3b,c] Moreover, the stability against UV light in air is also improved in the case of PETMP modified devices, as shown in Figure S4 (Supporting Information). To exclude a possible effect from the thickness of the modification layer caused by differences in the volatility of the modifier, the stability of EMP modified devices is studied for different EMP concentrations (from 0.2 – 0.8 mg mL^{-1}). As seen in Figure S5 (Supporting Information), the modified solar cells show a slightly slowed degradation even at the highest EMP concentration. Thus, the number of sulfhydryl groups plays an important role in the interfacial passivation.

GIWAXS/GISAXS measurements can provide very valuable information about the inner active layer structure. However, classical ex situ measurements cannot contribute easily to an understanding of kinetic processes for such a device degradation as *operando* measurement does.[3a–c,17] There is no heat effect from the X-ray beam accelerating the degradation since there is no continuous illumination with the X-ray beam. The GIWAXS and GISAXS measurements are carried out at beamline P03 (DESY, Hamburg) to observe the detailed degradation process of the stability-enhanced solar cells (see Figure S6, Supporting Information). Simultaneously, with the measurement of *J-V* curves under illumination with AM1.5 light, the GIWAXS/GISAXS data are taken at the film area between the two electrodes. Figure S7 (Supporting Information) shows the background GIWAXS data from the ZnO/ITO sample, where the two intensity rings at q positions of 0.28 $Å^{-1}$ and 0.52 $Å^{-1}$ are the signals of the Kapton windows, which is subtracted as background in the later analysis. Here, we focus on PETMP modified solar cells in comparison with the reference solar cell and shorten the measurement time scale due to the limited beamtime at synchrotron facilities. **Figure 3**a,b show the operando *J-V* curves of the reference solar cell and of the PETMP modified solar cell. Similar degradation behavior is also observed as Figure 2, where the loss of J_{SC} and FF is the main cause of the performance decrease, while V_{OC} just shows a slight decrease for the reference cell. As expected from the aging studies, the PETMP modified solar cell shows much better stability in all three device parameters (V_{OC}, J_{SC}, FF) against light degradation in air. Figures S8 and S9 (Supporting Information) show the 2D GIWAXS data from the operando experiments and Figure 3c,f compare the 2D GIWAXS data of the fresh/aged solar cells directly to illustrate the level of changes for the reference solar cell versus the PETMP modified solar cells. For the further analysis of the 2D GIWAXS data we focus on two directions: out-of-plane (OOP) direction referring to vertical cake cuts and in-plane (IP) direction referring to horizontal cake cuts. The peak in 2D GIWAXS data at q position around 1.70 $Å^{-1}$ in the OOP direction refers to the π-π stacking (010) with a face-on crystallite structure. Two lamellar stacking peaks (100) are seen at q of 0.32 $Å^{-1}$ in the IP and OOP direction, which refer to edge-on and face-on crystallite structures, respectively. The π-π stacking in OOP direction is of importance since face-on crystallites plays a favorable role in the charge transport as well as device performance.

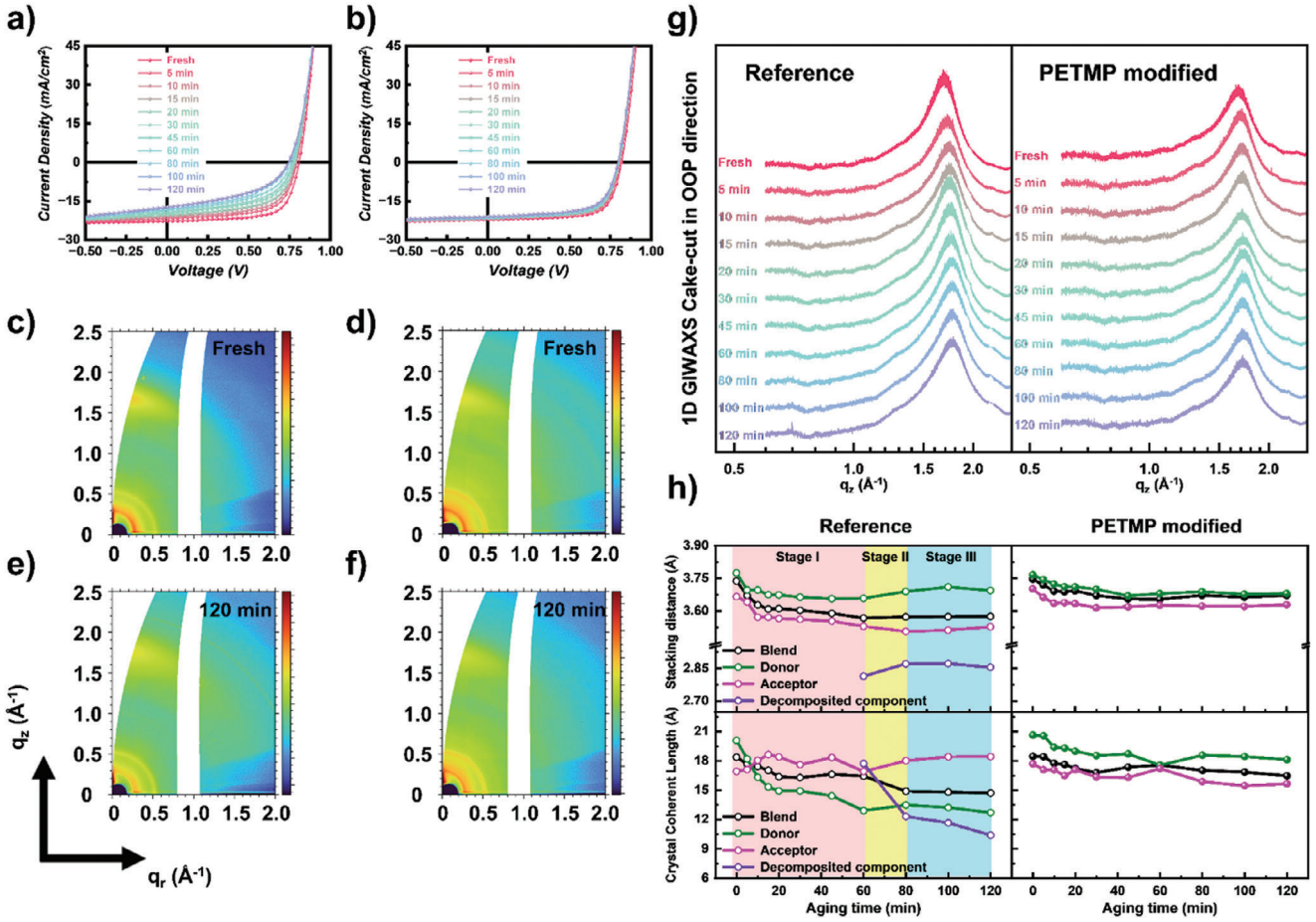

Figure 3. Temporal evolution of *J-V* curves of the a) reference and b) PETMP modified solar cells measured in situ with GIWAXS during illumination. 2D GIWAXS data of the c) fresh and e) aged reference solar cell and 2D GIWAXS data of the d) fresh and f) aged PETMP modified solar cell from the in situ studies. g) Cake cuts in OOP direction of the in situ 2D GIWAXS data of the reference (left) and PETMP modified solar cell (right). h) Temporal evolution of fit parameters (*d* and CCL) from the GIWAXS data analysis.

PETMP modification significantly stabilizes the crystallinity of the active layer in solar cells, as evidenced by the less pronounced shift in the π-π stacking signal after aging compared to the reference cell, with detailed *d* (*d*) and crystalline coherence length (L_C) calculations further supporting this observation. Figure 3g depicts cake cuts of the 2D GIWAXS data performed in the OOP directions of the reference solar cell and of the PETMP modified solar cell, where the background has been subtracted. The signal of the π-π stacking (010) for the reference solar cell shifts from 1.67 Å^{-1} to 1.77 Å^{-1} after 2 hours of aging, while it shifts less pronounced (1.68 Å^{-1} to 1.71 Å^{-1}) for the PETMP modified one, suggesting that the PETMP modification stabilizes the crystallinity of the active layer. For a further analysis of the GIWAXS data, the *d* and L_C are calculated for the π-π stacking in the OOP direction by[18]

$$d = \frac{2\pi}{q} \quad (1)$$

$$L_C = \frac{2\pi k}{FWHM} \quad (2)$$

where k is the Scherrer factor (k = 0.9), and *FWHM* is the full width at the half-maximum of the peak.[19] For the reference film without interfacial modification, the evolution can be divided into three stages (see Figure 3h). In the first stage, the *d* and L_C values decrease gradually from 3.74 Å and 18.38 Å to 3.57 Å and 16.43 Å in the first 60 minutes, respectively. This finding suggests a decrease in the crystallinity and molecular aggregation of the materials as well as the compressed crystal structure with aging, which might come from the decomposition of side chains or end groups in the donor/acceptor materials, as found in other previous work.[7c,14]

In the second stage, after 60 minutes of aging, the *d* value remains constant while the L_C value shows a sharp decrease to 14.89 Å. Finally, both *d* and L_C values remain constant, which is defined as the third stage. In contrast, for the PETMP modified case, the general *d* and L_C values decrease gradually from 3.75 Å and 18.45 Å to 3.67 Å and 16.47 Å, respectively, and no degradation stages are identified. Importantly, the relative changes of the parameters *d* and L_C are much less than those of the reference solar cell, illustrating the suppressed degradation with PETMP modification. For comparison, the evolution of the PETA modified case is also investigated by ex situ characterizations as

shown in Figure S10 (Supporting Information), where the general d value decreases from 3.72 Å to 3.60 Å, suggesting that it has no stability effect as indicated in the device degradation curves (Figure 2). Another point needing clarification is that, in general, a decreased d value will enhance the intermolecular interaction and consequently improve the charge transport and thereby consequently affect the device performance. However, here, such an evolution during aging is attributed to the collapse of the structure due to the decomposition of materials. Moreover, the peaks are separated into several peaks with different q positions. To understand such peak splitting, the pure films of donor polymer PBDB-TF-T1 and acceptor molecule BTP-4F-12 are measured with GIWAXS as well (see Figure S11, Supporting Information). Cake cuts in the OOP direction show peaks located at 1.68 $Å^{-1}$ for the donor polymer and 1.73 $Å^{-1}$ for the acceptor molecule (see Figure S12, Supporting Information), which are in agreement with the literature.[20] The corresponding stacking distances and crystalline coherence lengths are also shown in Figure S12 (Supporting Information). The acceptor shows a more intense π-π stacking than the donor, which is in agreement with the literature as well.[21] For further analysis, the peaks are fitted with Gaussian peaks as shown in Figures S13 and S14 (Supporting Information). We need three to four Gaussian peaks to model the measured π-π stacking peak shape. At the beginning of the operando GIWAXS study, all fit parameters are very similar for the reference, and PETMP modified solar cells, indicating the only small difference in the performance of the fresh devices. One peak at a q position of 1.38 $Å^{-1}$ always exists, which might come from the amorphous region of the acceptor and thus is not related to the π-π stacking that we are interested in and almost remains constant during the aging.[22]

L_C values, as well as the stacking distances, are calculated from the fit values and plotted in Figure 3h. The detailed values are listed in Tables S2 and S3 (Supporting Information). For the fresh blend film, the stacking distances and L_C values show combined results of the values for donor and acceptor, which is consistent with a former report.[21a] To be specific, the stacking distances of donor and acceptor increase from 3.74 Å and 3.63 Å to 3.78 Å and 3.69 Å, respectively, indicating a more intense π-π stacking formed in the blend, which can be beneficial for the charge transfer and device performance.[23] While the L_C value for donor and acceptor in the blend film (20.08 Å and 16.92 Å) shows a slight decrease compared to the pure materials (23.31 Å and 21.34 Å). The values for the PETMP modified case and the reference case are almost the same, indicating that the improved performance comes from an interfacial modification rather than from changes in the crystalline parts of the active layer. For the reference solar cell case, the L_C value of the donor decreases from 20.08 Å to 12.71 Å, while the L_C value of the acceptor remains relatively constant around 17 – 18 Å, which is disadvantageous for the charge transport characteristics.[24] The stacking distance of the donor and acceptor gradually decrease from 3.78 Å and 3.67 Å to 3.69 Å and 3.53 respectively, where the acceptor accounts for a relatively larger proportion to the overall π-π stacking signal, which might come from the collapsed structures due to the broken end groups.[7c,25]

In addition, a new feature arises at a q position of 2.25 $Å^{-1}$ ($d_{\pi\text{-}\pi} \approx 2.8$ Å) with a similar L_C value of the acceptor (17.72 Å) after aging for 60 minutes, i.e., in the second degradation stage, where the L_C value decreases quickly from 17.72 Å to 10.39 Å and the relative proportion increases by degrees from 7.45 to 16.05%. The ratios of the proportion of donor and acceptor ($S_{\pi\text{-}\pi.D}/S_{\pi\text{-}\pi.A}$) remain consistent during aging, which is similar to their weight ratio (1:1.2), demonstrating the reliability of the fit results. The arising feature observed here is attributed to a new component, which might come from the decomposition of the acceptor. For the data of the PETMP modified solar cell, the same analysis is carried out. The L_C value of the donor shows much less change compared to the reference, demonstrating that the PETMP modification is beneficial for the stability of the crystallinity of the donor polymer. The L_C value of the acceptor shows a similar evolution as the reference. No new feature is evolving, suggesting that PETMP can suppress the decomposition of the acceptor, which is consistent with our previous findings.[7c] The stacking distance of the donor shows the same decrease as the reference from 3.77 Å to 3.68 Å, whereas the stacking distance of the acceptor shows less decrease from 3.70 Å to 3.63 Å. This finding further indicates the effect of the PETMP modification on the acceptor.

PETMP modification has been proved to suppress changes in the stacking distances as well as L_C values for π-π stacking in the OOP direction, which is more crucial for the acceptor. In addition, also cake cuts in the IP direction are performed with the background subtracted, which includes the information about the lamellar stacking of face-on oriented crystallites (see Figure S15, Supporting Information). Two peaks assigned to the acceptor and donor are found at q positions of 0.28 $Å^{-1}$ and 0.32 $Å^{-1}$ respectively, where the stacking distances are 22.44 Å and 19.63 Å. The attribution of these peaks is referred to the literature.[21b] The peak positions and shapes remain stable during the aging. In more detail, the relative intensity of donor/acceptor signals shows an obvious increase, which might come from the decomposition of the acceptor thereby lowering its signal in the IP direction. In contrast, the lamellar stacking remains stable for the PETMP solar cell, suggesting a relatively more stable molecule stacking in the active layer with the applied interfacial modification.

To understand the changes in the active layer morphology, besides GIWAXS also *operando* GISAXS measurements are carried. The characteristic scattering pattern of the bottom part of the solar cells (ZnO/ITO substrate) is shown in Figure S16 (Supporting Information), together with the scattering of the active layer. The critical angle (α_c) of active layer materials is calculated to be 0.135° for pure PBDB-TF-T1 and 0.132° for pure BTP-4F-12 for the X-ray wavelength (1.044 Å), which is consistent with the calculation for PM6 and Y6 as previously reported.[26] At the critical angle, the Yoneda peak is located, as illustrated in Figure S16 (Supporting Information). From the GISAXS study, selected 2D GISAXS data of fresh and aged solar cells are shown in **Figure 4a,f**. More operando 2D GISAXS data of the reference and PETMP modified solar cell are seen in Figures S17 and S18 (Supporting Information), respectively. Horizontal line cuts of the 2D GISAXS data are taken at the Yoneda peak of 0.56 nm^{-1} (see Figure 4g). These data are modeled by assuming three cylindrically-shaped object types (domains) in the blend films with different radii (large, middle, and small).[27] The modeling is done in the framework of the distorted-wave Born approximation (DWBA) and the effective interface approximation (EIA), where

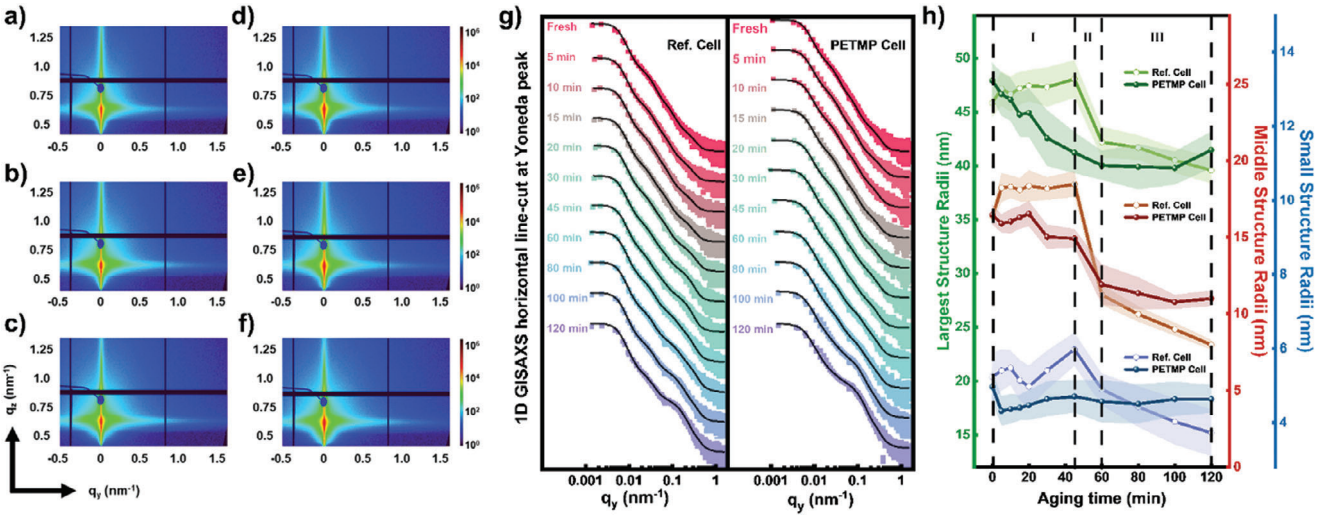

Figure 4. 2D GISAXS data of the a) fresh, b) 60 minutes aged and c) 120 minutes aged reference solar cell and 2D GISAXS data of the d) fresh, e) 60 minutes aged and f) 120 minutes aged PETMP modified solar cell from the operando studies. g) Horizontal line cuts of the in situ 2D GISAXS data taken at the Yoneda peak of active layer materials. h) Temporal evolution of characteristic radii of the three structures used to fit the horizontal line cuts.

a Gaussian size distribution is assumed to account for the polydispersity of the domains.[28]

Figure 4h summarizes the morphology changes during operation in terms of changes in the domain radii of the three types. It is challenging to attribute these domains to a specific donor or acceptor phase due to their similar electron densities. The two smaller object types are considered more crucial for the device performance since their dimensions are closer to the exciton diffusion length of active layer materials.[3c] The radius of the largest domain type decreases to rather similar values for the reference and PETMP modified solar cells after aging, although with different temporal trends. The radius of the middle domain type follows a similar trend and also decreases in both cases. However, in the PETMP modified case, the decrease is not as strong as in the reference solar cell. For the radius of the small domain type, a decrease is only found for the reference solar cell and the PETMP modified one shows main no changes on this length scale. Interestingly, the same three stages can also be defined in the GISAXS measurements during the degradation process. The similar degradation stages further confirm our understanding from the GIWAXS data analysis. Not only crystallinity and molecular aggregation of the materials are decreased, but also the domain sizes are decreased due to the compressed structures from the decomposition of the active layer materials. To be specific, such an evolution is particularly significant in the second stage, where the sharp change after aging for 60 minutes seen in GISAXS corresponds to the sharp change of L_C as well as generated the new material detected in the GIWAXS measurements. The decomposed component is not detected in GISAXS, which tells that it does not form regular domains within the resolved length scale regime. One of the possible reasons for the decreased domain sizes, especially at the beginning of the degradation, is the evaporation of the residual solvent additive as it was observed in the case of NFA based solar cells already.[3b,29] This explains well why the evolution trends for these two cases are almost same in the first stage. For the second stage, the difference mainly comes from the interface, where more collapsed structures are found in the reference case without PETMP modification.[7c,25] In addition, the ex-situ results of the PETA modified case are also investigated as shown in Figure S19 (Supporting Information), where the dimensions of the three domains decrease from 44.5 ± 1.5 nm, 18.2 ± 0.9 nm, 4.8 ± 0.3 nm to 39.6 ± 1.7 nm, 11.5 ± 0.7 nm, 3.8 ± 0.3 nm, respectively. Thus, similar decrease trends are observed as for the reference case. Combined with the GIWAXS results, there is no obvious difference in the evolution trend of the PETA films compared with the reference case, suggesting that its accelerated degradation might come from some other interfacial issues.

To confirm our aforementioned speculation and elaborate clearer, the surface properties are investigated further. Figure S20 (Supporting Information) shows AFM images of the ZnO surfaces modified with MeOH, EMP (0-SH) and PETMP (4-SH). Basically, we see no change either in the surface morphology or in the surface roughness for the different interfacial modifiers. XPS of the ZnO surface is conducted to analyze the element distribution. **Figure** 5a shows the O 1s peaks as seen in the XPS spectra of pure ZnO compared to the different interfacial modifiers. The O 1s peak contains three contributions. The low-binding energy marked in green (529.7 eV) refers to the ZnO lattice oxygen. The medium-binding energy marked in red (531.1 eV) refers to vacant oxygen or O 1s electrons from water molecules strongly bound to the exposed ZnO surface. The high-binding energy in blue (532.3 eV) refers to the oxygen from hydroxide or hydroxyl radicals, which would cause the decomposition of the acceptor and degradation of the solar cells, as reported in previous works.[30]

In earlier work, such an interfacial hydroxide or hydroxyl radical was further found to cause a fracturing down of the C=C bond of the acceptor and thus decrease the device performance, whereas the β-alkyl chains on the thiophene unit next to the C=C linker could block the attack of hydroxyl radicals onto the C=C bonds.[14] Figure 5b summarizes the ratio of these three kinds of oxygen. The proportion of hydroxide oxygen increases from

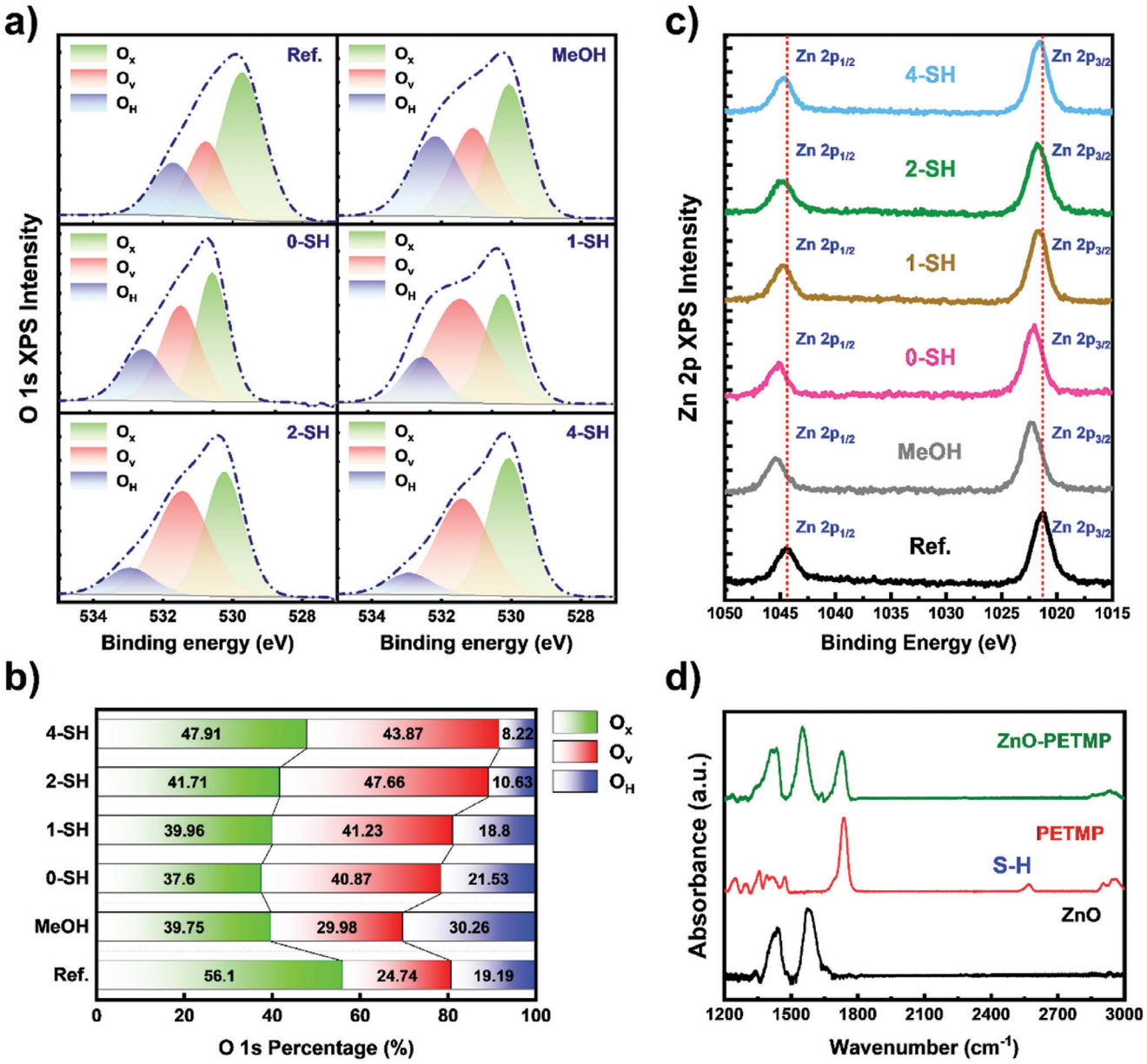

Figure 5. a) XPS spectra of O 1s peak at the surface of ZnO with different modifiers; b) comparison of the content of three kinds of oxygen of in the analysis of the XPS spectra of O 1s orbital; c) XPS spectra of Zn 2p peaks at the surface of ZnO with different modifiers, d) FTIR spectra of ZnO, PETMP and the mixture films.

19 to 30% with the modification via MeOH, and it decreases to 8% in the case of PETMP modification. The effective suppression of hydroxide oxygen via the mercapto derivatives is regarded as the reason for the observed enhanced interfacial stability, which is consistent with our previous conclusion.[7c] Interfacial passivation is another possible effect for the improved performance and stability, while it is challenging to further analyze, if such a modification effect is related to the passivation of oxygen vacancies from the XPS results, since the signal of vacant oxygen is overlapping with that of oxygen in the modifiers (531.1 eV). The suppression of hydroxide or hydroxyl radicals at the surface has been confirmed as the main degradation reason. The correlation between the number of sulfhydryl groups and the strength of the modification effect is supposed to be related to the interaction between Zn and S. Figure 5c depicts the XPS signal of Zn 2p peaks. The observed two peaks refer to Zn 2p 1/2 (1044.4 eV) and Zn 2p 3/2 (1021.4 eV), respectively.[31] These two peaks shift to higher energies of 1045.3 eV and 1022.3 eV with the MeOH modification, suggesting a change of the chemical environment of Zn. Such a shift is attributed to the increased electron density around Zn due to the existence of -OH groups at the ZnO surface. No significant shift of the peaks is observed in the PETA (0-SH) modification case compared with MeOH modified ZnO, suggesting no correlation between the PETA modifier and ZnO. In contrast,

the ZnO 2p peaks show strong shifts to 1044.6 eV and 1021.6 eV for the other three mercapto-containing modifiers, suggesting a change in the chemical environment of Zn coming from the interaction with sulphur in the modifier molecules. These peak positions show a tiny shift toward higher binding energy compare with the ZnO case, further proving the coordination between Zn and S, which would slightly cause the increased electron density of Zn.

In addition, FTIR measurements are performed for ZnO, PETMP, as well as their blend films, as shown in Figure 5d. The peak at around 2570 cm^{-1} is regarded as the signal of the S—H bond according to the literature, which disappears in the ZnO-PETMP blend film, suggesting the existence of coordination between Zn and S.[32] It can be concluded that such a coordination between Zn and S helps to suppress the hydroxide oxygen formation. Also, the modification can be more effectively with having more SH groups at a similar layer thickness. Obviously, mercaptans such as PETMP can offer the same effect for an enhanced stability like 2-PET does. These findings agree well with our previous work, where a clearer mechanism was proposed. In addition, it can be concluded from our previous knowledge that such a degradation starts with the decomposition of materials at the ZnO/active layer interface, followed by the evolution of the molecular packing as well crystallinity of the active layer internal materials. The interfacial modification of the underlying mercaptan layer suppresses the original degradation, and then influences the evolution in the bulk. In a word, such an interface degradation coming from hydroxide radicals will cause changes of the crystallinity and microstructure in the active layer, while a proper modification can suppress the hydroxide radical formation and thus improve device stability.

3. Conclusion

The sensitive interface of ZnO is quite crucial for organic solar cell performance and stability. Here, several mercaptan derivatives are explored as the interface modification material in green-solvent-based PBDB-TF-T1:BTP-4F-12 solar cells to investigate their effect on the device performance as well as light-stability in air. The changes in the structure and morphology of the active layer are investigated with operando GIWAXS and GISAXS measurements. Importantly, both the crystallinity and the microstructure of the active layer change during the device degradation, and the interfacial modification impacts the degree of degradation. The degradation of the reference solar cell without interfacial modification can be divided into three stages. In the first stage, the crystallinity of the polymer donor weakens gradually and the domain sizes stay relatively stable. In the second stage, due to the decomposition of the acceptor molecules, a new material appears after 60 minutes of aging, and the domain sizes decrease sharply. Finally, the crystallinity and stacking distance remain stable while the domain sizes continue decreasing. Such staged degradation would be easily ignored in simple ex situ measurements, while they contribute to the instability of the reference solar cells and are observable in the operando GIWAXS and GISAXS measurements. The enhanced device stability realized by the PETMP modification is based on impacting donor and acceptor materials. Upon PETMP modification, the crystallinity of the polymer donor is stabilized and the decomposition of the acceptor molecule is suppressed, resulting in an enhanced stability against light-induced degradation. Furthermore, it is found that the interfacial modification effect is related to the coordination between S and Zn, where the mercapto-rich modifiers can decrease the hydroxide oxygen at the interface, which causes the acceptor decomposition. Such findings deeply contribute to an understanding of the complex mechanisms of active layer degradation, where the inner structure of the active layer is also affected by the interfacial degradation at the ZnO interface. The stability improvement with hydroxide scavengers can serve not only for suppressing the decomposition of the acceptor as we knew before but also contribute to the stability of the crystallinity of the donor polymer.

4. Experimental Section

Materials: The patterned ITO substrates were bought from Liaoning Youxuan New Energy Technology Co., Ltd. The substrates were ultrasonically cleaned in the sequence of diluted Hellmanex III (2:98), DI water, acetone, and isopropanol consecutively for 30 minutes each before use. Cleaned ITO substrates were then flow-dried and treated by an O_3-plasma for spin-coating.

The ZnO nano-particles solution was synthesized as reported, which keeps consistent with the previous work.[33] The concentration of ZnO was 15 mg mL^{-1} in methanol with 0.05% (volume fraction) ethanolamine for better dispersion. The solution was spin-coated on the cleaned ITO substrates with a speed of 3000 rpm, resulting an optimized ZnO thickness of 30 to 40 nm. The as-cast ZnO films were then annealed at 130 °C for 10 minutes.

PBDB-TF-T1 and BTP-4F-12 were purchased from 1-Material Inc. THF (99.9%) and DPE (99.9%) were bought from Sigma-Aldrich Inc. The blend solution of PBDB-TF-T1 and BTP-4F-12 with 0.5 vol% DPE in THF was stirred for 3 h (the concentration of PBDB-TF-T1 and BTP-4F-12 was 18 mg mL^{-1} in total). The solution was dynamically spin-coated on the ZnO substrates with a speed of 2000 rpm, resulting in an optimized active layer thickness around 100 nm. The as-cast films were then annealed at 100 °C for 10 minutes.

MoO_3 and silver were bought from Carl Roth GmbH + Co. KG. MoO_3 was thermally evaporated on the active layer with a thickness of 10 nm. Silver was then evaporated on the top with a thickness of 100 nm. Both evaporations were conducted under a vacuum of 3×10^{-6} Pa.

Characterizations: *J-V* measurements were carried out with a solar simulator (class ABA, Newport) with a lamp (SMR-100/XEAR2, Ushio America, Inc.) as the light source and 2611B Keithley as the monitor of voltage and current. The light intensity was corrected with a reference silicon solar cell (Fraunhofer ISE019-2015) before measurement and set at 100 mW cm^{-2}. The solar cell devices were measured by masking the active area with a metal mask of 0.079 cm^2.

Stability measurements (as well as *operando J-V* measurements) were carried out with a homemade system called "pocket solar", which adapts a lamp (PE150AF Xenon Ceramic Body Parabolic Lamp) to mimic the solar spectrum. The atmosphere temperature during the measurement was controlled at 25 °C via a Julabo to exclude the possible effects from heat. The light intensity was adjusted to 100 mW cm^{-2} as AM 1.5G with a reference silicon solar cell (Fraunhofer ISE019-2015) before the measurements. The *J-V* sweeps ran every two minutes and the parameters (V_{OC}, J_{SC}, FF, PCE) were calculated automatically.

Atomic Force Microscope (AFM) measurements were carried out with an AFM instrument (Nanosurf, FlexAFM, Switzerland). Gwyddion was used as the software for data analysis and image post-processing.[34]

X-ray photoelectron spectroscopy (XPS) spectra were measured through PHI 5000 Versa Probe III at the Vacuum Interconnected Nanotech Workstation (Nano-X) of SINANO.

Fourier-transform infrared spectroscopy (FTIR) spectra were collected from a FT-IR spectrometer (Bruker Equinox), where the films were drop-casted on cleaned silicon wafers.

Operando GIWAXS/GISAXS experiments were conducted at the PETRA III synchrotron P03 beamline at Deutsches Elektronen-Synchrotron (DESY, Hamburg). A monochromatic X-ray beam with an energy of 11.7 keV and a beam size of $23 \times 32\ \mu m^2$ was used. Alignment was carried out every 15 minutes to ensure the accuracy of the incidence angle. A damage scan was conducted before the operando measurements and a damage of the organic materials was found after 5 seconds of X-ray exposure. Therefore, the individual X-ray beam exposure time per spot were limited to be well below this damage time by moving the sample in the beam (10 µm each step). The positions of the X-ray beam center and sample-to-detector distance (SDD) in all measurements using a LAMBDA 9 M (X-Spectrum, pixel size 55 µm) detector were calibrated by fitting the patterns of LaB_6 and CeO_2 with the DPDAK package.[35] The reshaped 2D GIWAXS data, as well as the cake cuts of the scattering data, were processed with the Python tool INSIGHT.[36] The 2D GISAXS data were generated with BornAgain (version 1.17.0).[37] The line cuts of the 2D GISAXS data were also done with the DPDAK package and fitted in the framework of the distorted-wave Born approximation (DWBA) and the effective interface approximation (EIA) with a lab fitting tool. For GISAXS, the samples were probed at an incidence angle of 0.4° with a Pilatus 2 M (Dectris, pixel size 172 µm) detector in an SDD of 4242 mm to study the sample morphology on the micro-scale. The exposure time for each GISAXS image was 1 s. For GIWAXS, the samples were probed at an incidence angle of 0.13° and 0.6° with an SDD of 164 mm to study the sample crystallinity. The exposure time for each GIWAXS image was 1 s. The scattering signal of ITO was obtained from the GIWAXS data measured at 0.6°, and the correction of the SDD values was done by calibrating the ITO peaks to $q = 2.132\ Å^{-1}$, which was determined before from the XRD measurement of the same batch ITO substrate.

Supporting Information

Supporting Information is available from the Wiley Online Library or from the author.

Acknowledgements

This work was supported by funding from the Deutsche Forschungsgemeinschaft (DFG, German Research Foundation) Grant No. Mu1487/22 and under Germany's Excellence Strategy – EXC 2089/1 – 390776260 (e conversion) and via International Research Training Group 2022 Alberta/Technical University of Munich International Graduate School for Environmentally Responsible Functional Materials (ATUMS), TUM.solar in the context of the Bavarian Collaborative Research Project Solar Technologies Go Hybrid (SolTech) and the Center for NanoScience (CeNS). Z.L., J.Z., R.G., K.S., X.J., S.T., and P.W. acknowledge the China Scholarship Council (CSC). All GIWAXS/GISAXS measurements were carried out at the light source PETRA III at DESY, a member of the Helmholtz Association (HGF). Z.L., Y.L, and C.M. were grateful for the technical support for Nano-X from Suzhou Institute of Nano-Tech and Nano-Bionics, Chinese Academy of Sciences.

Conflict of Interest

The authors declare no conflict of interest.

Data Availability Statement

The data that support the findings of this study are available from the corresponding author upon reasonable request.

Keywords

degradation, device stabilization, GISAXS/GIWAXS, non-fullerene organic solar cells, studies

Received: July 4, 2024
Revised: August 9, 2024
Published online:

[1] a) C. Han, J. Wang, S. Zhang, L. Chen, F. Bi, J. Wang, C. Yang, P. Wang, Y. Li, X. Bao, *Adv. Mater.* **2023**, *35*, 2208986; b) J. Wang, Y. Wang, P. Bi, Z. Chen, J. Qiao, J. Li, W. Wang, Z. Zheng, S. Zhang, X. Hao, J. Hou, *Adv. Mater.* **2023**, *35*, 2301583.
[2] a) L. Duan, A. Uddin, *Adv. Sci.* **2020**, *7*, 1903259; b) Y. Zhang, Y. Lang, G. Li, *EcoMat.* **2023**, *5*, 12281.
[3] a) K. S. Wienhold, W. Chen, S. Yin, R. Guo, M. Schwartzkopf, S. V. Roth, P. Müller-Buschbaum, *Sol. RRL.* **2020**, *4*, 2000251; b) D. Yang, F. C. Löhrer, V. Körstgens, A. Schreiber, S. Bernstorff, J. M. Buriak, P. Müller-Buschbaum, *ACS Energy Lett.* **2019**, *4*, 464; c) D. Yang, F. C. Löhrer, V. Körstgens, A. Schreiber, B. Cao, S. Bernstorff, P. Müller-Buschbaum, *Adv. Sci.* **2020**, *7*, 2001117; d) C. Wang, J. Lai, Q. Chen, F. Zhang, L. Chen, *Nano Lett.* **2021**, *21*, 8474; e) R. Pandya, A. Mathieson, B. D. Boruah, H. B. de Aguiar, M. de Volder, *Nano Lett.* **2023**, *23*, 7288.
[4] a) C. Liu, C. Xiao, W. Li, *J. Mater. Chem. C.* **2021**, *9*, 14093; b) N. Ahmad, H. Zhou, P. Fan, G. Liang, *EcoMat.* **2022**, *4*, 12156.
[5] L. Y. Su, H. H. Huang, Y. C. Lin, G. L. Chen, W. C. Chen, W. Chen, L. Wang, C. C. Chueh, *Adv. Funct. Mater.* **2021**, *31*, 2005753.
[6] H. Li, B. Yu, H. Yu, *Adv. Funct. Mater.* **2024**, 2402128.
[7] a) Y. Jiang, L. Sun, F. Jiang, C. Xie, L. Hu, X. Dong, F. Qin, T. Liu, L. Hu, X. Jiang, *Mater. Horiz.* **2019**, *6*, 1438; b) S. Park, H. J. Son, *J. Mater. Chem. A.* **2019**, *7*, 25830; c) B. Liu, Y. Han, Z. Li, H. Gu, L. Yan, Y. Lin, Q. Luo, S. Yang, C.-Q. Ma, *Sol. RRL.* **2021**, *5*, 2000638.
[8] a) H. Liu, Z. X. Liu, S. Wang, J. Huang, H. Ju, Q. Chen, J. Yu, H. Chen, C. Z. Li, *Adv. Energy Mater.* **2019**, *9*, 1900887; b) X. Xu, J. Xiao, G. Zhang, L. Wei, X. Jiao, H.-L. Yip, Y. Cao, *Sci. Bull.* **2020**, *65*, 208.
[9] A. Soultati, A. Verykios, S. Panagiotakis, K.-K. Armadorou, M. I. Haider, A. Kaltzoglou, C. Drivas, A. Fakharuddin, X. Bao, C. Yang, A. R. b. M. Yusoff, E. K. Evangelou, I. Petsalakis, S. Kennou, P. Falaras, K. Yannakopoulou, G. Pistolis, P. Argitis, M. Vasilopoulou, *ACS Appl. Mater. Interfaces.* **2020**, *12*, 21961.
[10] M. Günther, D. Blätte, A. L. Oechsle, S. S. Rivas, A. A. Yousefi Amin, P. Müller-Buschbaum, T. Bein, T. Ameri, *ACS Appl. Mater. Interfaces.* **2021**, *13*, 19072.
[11] a) J. Yuan, Y. Zhang, L. Zhou, G. Zhang, H.-L. Yip, T.-K. Lau, X. Lu, C. Zhu, H. Peng, P. A. Johnson, M. Leclerc, Y. Cao, J. Ulanski, Y. Li, Y. Zou, *Joule.* **2019**, *3*, 1140; b) Q. Liang, J. Han, C. Song, X. Yu, D.-M. Smilgies, K. Zhao, J. Liu, Y. Han, *J. Mater. Chem. A.* **2018**, *6*, 15610; c) Q. Fan, Q. Zhu, Z. Xu, W. Su, J. Chen, J. Wu, X. Guo, W. Ma, M. Zhang, Y. Li, *Nano Energy.* **2018**, *48*, 413; d) Y. Deng, W. Li, L. Liu, H. Tian, Z. Xie, Y. Geng, F. Wang, *Energy Environ. Sci.* **2015**, *8*, 585; e) X. Dong, Y. Deng, H. Tian, Z. Xie, Y. Geng, F. Wang, *J. Mater. Chem. A.* **2015**, *3*, 19928.
[12] a) Y. Cui, H. Yao, L. Hong, T. Zhang, Y. Xu, K. Xian, B. Gao, J. Qin, J. Zhang, Z. Wei, *Adv. Mater.* **2019**, *31*, 1808356; b) L. Hong, H. Yao, Z. Wu, Y. Cui, T. Zhang, Y. Xu, R. Yu, Q. Liao, B. Gao, K. Xian, H. Y. Woo, Z. Ge, J. Hou, *Adv. Mater.* **2019**, *31*, 1903441.
[13] X. Ma, J. Wang, J. Gao, Z. Hu, C. Xu, X. Zhang, F. Zhang, *Adv. Energy Mater.* **2020**, *10*, 2001404.
[14] B. Liu, X. Su, Y. Lin, Z. Li, L. Yan, Y. Han, Q. Luo, J. Fang, S. Yang, H. Tan, *Adv. Sci.* **2022**, *9*, 2104588.

[15] a) W. Lan, J. Gu, S. Wu, Y. Peng, M. Zhao, Y. Liao, T. Xu, B. Wei, L. Ding, F. Zhu, *EcoMat.* **2021**, *3*, 12134; b) C. Yang, S. Zhan, Q. Li, Y. Wu, X. Jia, C. Li, K. Liu, S. Qu, Z. Wang, Z. Wang, *Nano Energy.* **2022**, *98*, 107299.
[16] X. Jiang, A. J. Gillett, T. Zheng, X. Song, J. E. Heger, K. Sun, L. V. Spanier, R. Guo, S. Liang, S. Bernstorff, P. Müller-Buschbaum, *Energy Environ. Sci.* **2023**, *16*, 5970.
[17] a) R. Ma, X. Jiang, J. Fu, T. Zhu, C. Yan, K. Wu, P. Müller-Buschbaum, G. Li, *Energy Environ. Sci.* **2023**, *16*, 2316; b) M. Qin, P. F. Chan, X. Lu, *Adv. Mater.* **2021**, *33*, 2105290; c) T. Derrien, A. Lauritzen, P. Kaienburg, J. Hardigree, C. Nicklin, M. Riede, *J. Phys. Chem. C.* **2020**, *124*, 11863.
[18] a) J. Xu, F. Lin, L. Zhu, M. Zhang, T. Hao, G. Zhou, K. Gao, Y. Zou, G. Wei, Y. Yi, *Adv. Energy Mater.* **2022**, *12*, 2201338; b) L. Zhu, M. Zhang, G. Zhou, T. Hao, J. Xu, J. Wang, C. Qiu, N. Prine, J. Ali, W. Feng, *Adv. Energy Mater.* **2020**, *10*, 1904234; c) W. Zheng, J. Liu, Y. Guo, G. Han, Y. Yi, *Adv. Funct. Mater.* **2022**, *32*, 2108551; d) Y. Ma, D. Cai, S. Wan, P. Yin, P. Wang, W. Lin, Q. Zheng, *Natl. Sci. Rev.* **2020**, *7*, 1886; e) L. Ye, W. Zhao, S. Li, S. Mukherjee, J. H. Carpenter, O. Awartani, X. Jiao, J. Hou, H. Ade, *Adv. Energy Mater.* **2017**, *7*, 1602000.
[19] S. M. Hosseini, N. Tokmoldin, Y. W. Lee, Y. Zou, H. Y. Woo, D. Neher, S. Shoaee, *Sol. RRL.* **2020**, *4*, 2000498.
[20] F. T. A. Wibowo, N. V. Krishna, S. Sinaga, S. Lee, W. T. Hadmojo, Y. R. Do, S.-Y. Jang, *Cell Rep. Phys. Sci.* **2021**, *2*, 100517.
[21] a) Y. Chen, F. Bai, Z. Peng, L. Zhu, J. Zhang, X. Zou, Y. Qin, H. K. Kim, J. Yuan, L.-K. Ma, J. Zhang, H. Yu, P. C. Y. Chow, F. Huang, Y. Zou, H. Ade, F. Liu, H. Yan, *Adv. Energy Mater.* **2021**, *11*, 2003141; b) H. Lu, K. Chen, R. S. Bobba, J. Shi, M. Li, Y. Wang, J. Xue, P. Xue, X. Zheng, K. E. Thorn, I. Wagner, C.-Y. Lin, Y. Song, W. Ma, Z. Tang, Q. Meng, Q. Qiao, J. M. Hodgkiss, X. Zhan, *Adv. Mater.* **2022**, *34*, 2205926.
[22] a) Z. Yin, X. Guo, Y. Wang, L. Zhu, Y. Chen, Q. Fan, J. Wang, W. Su, F. Liu, M. Zhang, Y. Li, *Chem. Eng. J.* **2022**, *442*, 136018; b) L. Wang, J.-Z. Zhan, W.-K. Zhong, L. Zhu, G.-Q. Zhou, T.-Y. Hao, Y.-C. Zou, Z.-H. Wang, G. Wei, Y.-M. Zhang, F. Liu, *Chin. J. Polym. Sci.* **2023**, *41*, 842.
[23] a) Z. Gan, L. Wang, J. Cai, C. Guo, C. Chen, D. Li, Y. Fu, B. Zhou, Y. Sun, C. Liu, J. Zhou, D. Liu, W. Li, T. Wang, *Nat. Commun.* **2023**, *14*, 6297; b) W. Zhang, Y. Wu, R. Ma, H. Fan, X. Li, H. Yang, C. Cui, Y. Li, *Angew. Chem., Int. Ed.* **2023**, *62*, 202309713.
[24] L. Ye, W. Zhao, S. Li, S. Mukherjee, J. H. Carpenter, O. Awartani, X. Jiao, J. Hou, H. Ade, *Adv. Energy Mater.* **2017**, *7*, 1602000.
[25] Y. Jiang, L. Sun, F. Jiang, C. Xie, L. Hu, X. Dong, F. Qin, T. Liu, L. Hu, X. Jiang, Y. Zhou, *Mater. Horiz.* **2019**, *6*, 1438.
[26] G. Cai, Y. Li, Y. Fu, H. Yang, L. Mei, Z. Nie, T. Li, H. Liu, Y. Ke, X.-L. Wang, J.-L. Brédas, M.-C. Tang, X. Chen, X. Zhan, X. Lu, *Nat. Commun.* **2024**, *15*, 2784.
[27] S. Guo, W. Wang, E. M. Herzig, A. Naumann, G. Tainter, J. Perlich, P. Müller-Buschbaum, *ACS Appl. Mater. Interfaces.* **2017**, *9*, 3740.
[28] A. L. Oechsle, J. E. Heger, N. Li, S. Yin, S. Bernstorff, P. Müller-Buschbaum, *ACS Appl. Mater. Interfaces.* **2022**, *14*, 30802.
[29] C. J. Schaffer, C. M. Palumbiny, M. A. Niedermeier, C. Burger, G. Santoro, S. V. Roth, P. Müller-Buschbaum, *Adv. Energy Mater.* **2016**, *6*, 1600712.
[30] a) M. Chen, X. Wang, Y. Yu, Z. Pei, X. Bai, C. Sun, R. Huang, L. Wen, *Appl. Surf. Sci.* **2000**, *158*, 134; b) T. J. Frankcombe, Y. Liu, *Chem. Mater.* **2023**, *35*, 5468; c) P. Gu, X. Zhu, H. Wu, J. Li, D. J. J. o. A. Yang, *J. Alloys Compd.* **2019**, *779*, 821; d) J. T. Kloprogge, L. V. Duong, B. J. Wood, R. L. Frost, *J. Colloid Interface Sci.* **2006**, *296*, 572.
[31] L. Wang, B. Cheng, L. Zhang, J. Yu, *Small.* **2021**, *17*, 2103447.
[32] X. Zhang, S. Wang, *Sensors.* **2003**, *3*, 61.
[33] W. J. E. Beek, M. M. Wienk, M. Kemerink, X. Yang, R. A. J. Janssen, *J. Phys. Chem. B.* **2005**, *109*, 9505.
[34] D. Nečas, P. Klapetek, *Open Phys.* **2012**, *10*, 181.
[35] G. Benecke, W. Wagermaier, C. Li, M. Schwartzkopf, G. Flucke, R. Hoerth, I. Zizak, M. Burghammer, E. Metwalli, P. Müller-Buschbaum, M. Trebbin, S. Förster, O. Paris, S. V. Roth, P. Fratzl, *J. Appl. Crystallogr.* **2014**, *47*, 1797.
[36] a) M. A. Reus, L. K. Reb, A. F. Weinzierl, C. L. Weindl, R. Guo, T. Xiao, M. Schwartzkopf, A. Chumakov, S. V. Roth, P. Müller-Buschbaum, *Adv. Opt. Mater.* **2022**, *10*, 2102722; b) M. A. Reus, L. K. Reb, D. P. Kosbahn, S. V. Roth, P. Müller-Buschbaum, *J. Appl. Crystallogr.* **2024**, *57*, 509.
[37] G. Pospelov, W. Van Herck, J. Burle, J. M. Carmona Loaiza, C. Durniak, J. M. Fisher, M. Ganeva, D. Yurov, J. Wuttke, *J. Appl. Crystallogr.* **2020**, *53*, 262.